# Simulation of neutron emission in NBI-heated plasmas with the real-time code RABBIT

M. Weiland[1*], R. Bilato[1], C.S. Collins[2], W.W. Heidbrink[3], D. Liu[3], M.A. Van Zeeland[2], the ASDEX Upgrade, DIII-D and Eurofusion MST1 teams[†] and JET contributors[‡]

[1]Max-Planck-Institut für Plasmaphysik, Garching, Germany
[2]General Atomics, San Diego, California, USA
[3]Department of Physics and Astronomy, University of California, Irvine, California, USA

**Abstract**

In plasmas heated with deuterium beams a deficit of the expected fusion neutron rate is an indicator of the deterioration of the fast-ion confinement, caused, for instance, by magnetohydrodynamic instabilities. The capability of predicting this deficit during the discharge relies on the availability of real-time estimates of the neutron rate from NBI codes which must be fast and accurate at the same time. Therefore, the recently developed real-time RABBIT code for NBI simulations has been extended to output the distribution function and calculate the neutron emission. After the description of this newly installed diagnostics in RABBIT, benchmarks with NUBEAM, a massively used and validated Monte Carlo NBI solver, are discussed on ASDEX-Upgrade and JET cases. A first application for control-room intershot analysis on DIII-D is presented, and the results are compared on a large database with a slower NUBEAM analysis. Further application possibilities, e.g. for real-time control of Alfvén eigenmodes, are outlined.

## 1 Introduction

Neutrons are produced in hydrogenic plasmas by the following fusion reactions:

$$\mathrm{D} + \mathrm{D} \longrightarrow \begin{cases} {}^3\mathrm{He} + \mathrm{n} + 3.3\,\mathrm{MeV} & (50\%) \\ \mathrm{T} + \mathrm{p} + 4.0\,\mathrm{MeV} & (50\%) \end{cases} \tag{1}$$

$$\mathrm{D} + \mathrm{T} \longrightarrow {}^4\mathrm{He} + \mathrm{n} + 17.6\,\mathrm{MeV} \tag{2}$$

$$\mathrm{T} + \mathrm{T} \longrightarrow {}^4\mathrm{He} + 2\mathrm{n} + 11.3\,\mathrm{MeV} \tag{3}$$

Additional fusion reactions involving $^3$He are: $^3$He(d,p)$^4$He, $^3$He(t,p+n)$^4$He, $^3$He(t,d)$^4$He and $^3$He($^3$He,2p)$^4$He. In present-day devices, mostly pure deuterium discharges are carried out such that the DD reaction (1) is most relevant. The ion temperatures are often too low to create significant thermo-nuclear neutrons. However, in the presence of fast D ions, e.g. due to neutral beam injection (NBI), the neutron yield is significantly increased, because the fast ions have a high relative velocity with respect to the slow thermal bulk. Consequently, the so-called beam-target reactions between a fast and a thermal ion

*E-mail: markus.weiland@ipp.mpg.de
†see the author list of "H. Meyer et al, Nucl. Fusion 57, 102014 (2017)"
‡see the author list of "X. Litaudon et al, Nucl. Fusion 57, 102001 (2017)"

dominate the neutron emission. Measurements of the neutron emission (either total yield or spectrally resolved) can hence be used as a diagnostic for the fast ions.

Many experimental studies (e.g. [1–4]) have shown that in the absence of MHD instabilities or other anomalous transport mechanisms, the measured NBI fast-ion distribution is in good agreement with neoclassical predictions from e.g. the NUBEAM module [5, 6] in TRANSP [7]. Consequently, comparing measured neutron rates with a neoclassical prediction is an efficient tool to diagnose the fast-ion confinement. If there is a significant short-fall of the measurement versus the prediction, this gives a direct indication of fast-ion redistribution (e.g. due to too strong AE activity [8–11] or other fast-ion driven instabilities [1, 12, 13]) and overall poor discharge performance. It is desirable to have this information available directly after the discharge or even in real-time. In the first case, it can be incorporated in the planning of the following discharge and facilitate scenario development of e.g. advanced scenarios. In the second case, it can be even tried in real-time to counter-act the poor discharge performance, e.g. by stabilizing the MHD modes responsible for the neutron short-fall.

High fidelity NBI codes such as NUBEAM are clearly too slow for real-time applications. Recently, however, the real-time capable RABBIT code [14] has been developed which still shows good agreement with the NUBEAM code. In this paper, we discuss an extension of RABBIT to calculate neutron emission profiles from the plasma, in order to allow the aforementioned applications. A brief summary of the RABBIT code is given in section 2. In section 3, we review the necessary equations to calculate neutron rates and in section 4 we discuss the implementation. A benchmark case on the ASDEX Upgrade and JET tokamak is shown in section 5 and in section 6 we present an extensive test on DIII-D where RABBIT was already used in the control room for intershot analysis.

## 2 A brief summary of the RABBIT code

The fast-ion distribution function $f$ is described by the kinetic equation:

$$\frac{\partial f}{\partial t} + (\vec{v} \cdot \nabla_{\vec{x}} f + \vec{a} \cdot \nabla_{\vec{v}} f) = -\nabla_{\vec{v}} \cdot \vec{\Gamma}_{\mathrm{c}}(f) + \sigma \tag{4}$$

where the terms correspond (from left to the right) to the partial time derivative, the orbit effects, the collision operator and the source term (due to NBI injection). NUBEAM solves this equation using a Monte Carlo technique (and an additional sink term when the fast-ions have thermalized, i.e. slowed down to $3/2T_{\mathrm{i}}$). In order to be faster, RABBIT has to make several approximations, which are outlined in the following.

RABBIT uses a simplified NBI geometry. The attenuation is currently calculated along the center-line only, which gives good agreement with NUBEAM for the shine-through power. To calculate the birth profile, a semi-analytic beam width correction is applied in the poloidal plane, perpendicular to the beam center-line. An ad-hoc correction for finite orbit width effects is included by averaging the birth profile over the first fast ion orbit. The orbits are calculated with a conventional 4th order Runge-Kutta integrator. To still allow calculations in real-time, the orbit-average is calculated efficiently using only a low number of orbits (typically 20) along the beam-centerline. To gather the orbit information in between and off-axis to the center-line, an optimized inter- and extra-

polation scheme is used. The details of this approach are described in [14]. The kinetic equation eventually solved by RABBIT is:

$$\frac{\partial f}{\partial t} = -\nabla_{\vec{v}} \cdot \vec{\Gamma}_{\mathrm{c}}(f) + \langle \sigma \rangle (\rho, v, \xi) \tag{5}$$

where $\langle \dots \rangle$ denotes the average over the first orbit. The orbit-averaged source term $\langle \sigma \rangle$ is given as a function of radius $\rho$, speed $v$ and pitch $\xi = v_{\parallel}/v$. We assume a monoenergetic source with birth velocity $v_0$: $\langle \sigma \rangle = \frac{S(\rho,\xi)}{2\pi v^2}\delta(v - v_0)$. For different beams or different energy components of an individual beam, the equation can be solved independently and the different solutions can be added. The collision operator acts only in velocity space, such that the equation can be solved independently in each radial cell. In the following, we will therefore focus on the solution in a given radial cell, and will not write the $\rho$ dependencies explicitly for brevity of the notation. The collision operator is given by:

$$\begin{aligned} &- \nabla_{\vec{v}} \cdot \vec{\Gamma}_{\mathrm{c}}(f) = \\ &= \frac{1}{\tau_{\mathrm{s}} v^2} \frac{\partial}{\partial v}[(v^3 + v_{\mathrm{c}}^3) f] \; + \; \frac{\beta}{\tau_{\mathrm{s}}} \frac{v_{\mathrm{c}}^3}{v^3} \frac{\partial}{\partial \xi}(1 - \xi^2) \frac{\partial f}{\partial \xi} \; + \; \frac{1}{\tau_{\mathrm{s}} v^2} \frac{\partial}{\partial v} \left[ \left( \frac{T_{\mathrm{e}}}{m_{\mathrm{fi}}} v^2 + \frac{T_{\mathrm{i}}}{m_{\mathrm{fi}}} \frac{v_{\mathrm{c}}^3}{v} \right) \frac{\partial f}{\partial v} \right] \end{aligned} \tag{6}$$

with the slowing down, pitch angle scattering and speed diffusion term (from left to right). $v_c$ is the critical speed, $\tau_{\mathrm{s}}$ the Spitzer time, $\beta$ the pitch-angle scattering parameter and $m_{\mathrm{fi}}$ the mass of the fast-ion species [14].

The steady-state solution of this Fokker-Planck (FP) equation, which is 2D in velocity space, has been found in [15, 16]. Below the injection velocity ($v < v_0$), we neglect the speed-diffusion and get an infinite series of Legendre polynomials $P_l$:

$$f_-(v, \xi) = \frac{1}{2\pi} \frac{\tau_{\mathrm{s}}}{v^3 + v_{\mathrm{c}}^3} \cdot \sum_{l=0}^{\infty} \left(l + \tfrac{1}{2}\right) P_l(\xi) S_l \cdot \left( \frac{v_0^3 + v_{\mathrm{c}}^3}{v^3 + v_{\mathrm{c}}^3} \frac{v^3}{v_0^3} \right)^{\frac{\beta l(l+1)}{3}} \tag{7}$$

with $S_l$ being the Legendre components of the source ($S_l = \int S(\xi) P_l(\xi)\, \mathrm{d}\xi$).

Above the injection velocity ($v > v_0$) we neglect the pitch angle scattering and get a high-energy tail due to the speed diffusion in the vicinity of $v_0$ (i.e. assuming $v \approx v_0$):

$$f_+(v, \xi) = \frac{1}{2\pi} \frac{\tau_{\mathrm{s}}}{v_0^3 + v_{\mathrm{c}}^3} \cdot \sum_{l=0}^{\infty} \left(l + \tfrac{1}{2}\right) P_l(\xi) S_l \cdot \exp \frac{-(v^2 - v_0^2)}{v_{\mathrm{eff}}^2}, \tag{8}$$

$$v_{\mathrm{eff}}^2 = \frac{2}{m_{\mathrm{fi}}} \frac{T_{\mathrm{e}} v_0^3 + T_{\mathrm{i}} v_{\mathrm{c}}^3}{v_0^3 + v_{\mathrm{c}}^3} \tag{9}$$

We neglect the time-dependence for the high-energy tail $f_+$ and use this steady-state solution instantaneously.

For $f_-$ the time-dependence is treated as follows: We assume discrete time-steps $\Delta t$, during which we assume constant plasma parameters. Thanks to the neglection of speed diffusion, we can calculate how far fast ions will slow down during the time-step: $v_{\mathrm{final}}^3 = (v_{\mathrm{start}}^3 + v_{\mathrm{c}}^3) \cdot \exp \frac{-3 \cdot \Delta t}{\tau_{\mathrm{s}}} - v_{\mathrm{c}}^3$. As described in [14], the time-dependent solution is then given by a 'Heaviside-chunk' of the steady state solution:

$$f = f_- \cdot H(v - v_{\mathrm{final}}) \cdot H(v_{\mathrm{start}} - v) \tag{10}$$

i.e. the solution $f_-$ is only to be evaluated between $v_{\text{final}} < v < v_{\text{start}}$. This allows to setup a scheme of a fast-ion pulse train (as illustrated in fig. 1), where the final state during the previous time-step becomes the new source term $\langle\sigma\rangle$ for the following time-step. The distribution function is then given by a summation over all Heaviside-chunks in one time-step.

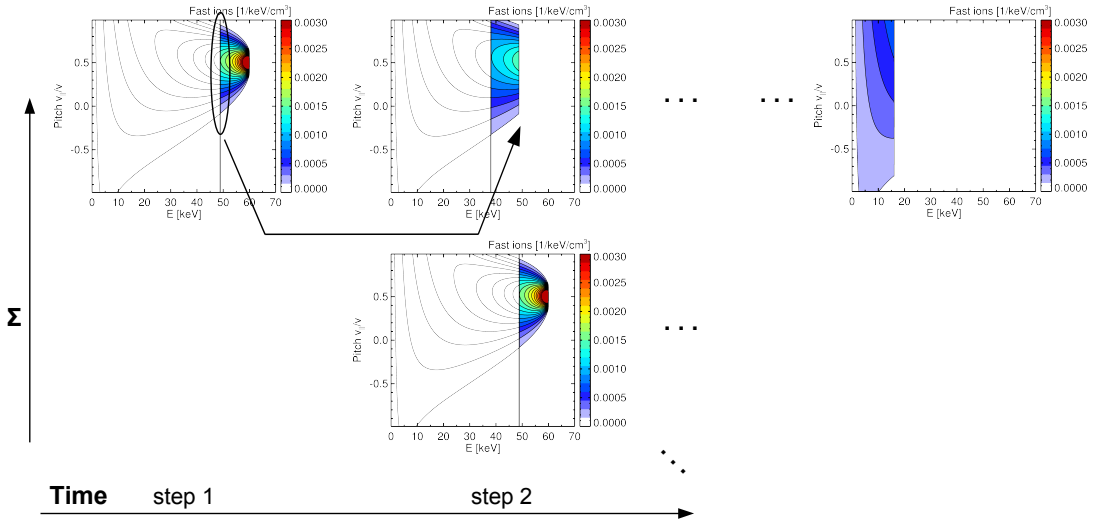


**Figure 1:** Time-dependence scheme of RABBIT. Columns correspond to time steps, and for each time step the rows are summed (indicated by the Σ symbol). This example assumes constant background plasma and constant beam power (switched on at time step 1). Reprint from [14].

It has been shown in [14] that this approach gives a very good agreement with NUBEAM results for heating profiles, fast-ion density and pressure profiles in ASDEX Upgrade benchmark cases. The agreement for beam driven currents was slightly inferior but still good. In the following, we will focus now on the calculation of neutron emission.

## 3 Calculation of neutron rates

The neutron emission rate caused by collisions between a species $\alpha$ and $\beta$ with distribution function $f$ is given by:

$$r = \frac{1}{1+\delta_{\alpha\beta}} \iint f_\alpha(\vec{v}_\alpha) f_\beta(\vec{v}_\beta) \cdot \sigma_{\alpha\beta}(v_{\text{rel}}) v_{\text{rel}} \, \mathrm{d}^3\vec{v}_\alpha \mathrm{d}^3\vec{v}_\beta \tag{11}$$

$$\text{with: } v_{\text{rel}} = |\vec{v}_\alpha - \vec{v}_\beta| \quad \text{and: } \delta_{\alpha\beta} = \begin{cases} 0 & \text{if } \alpha \neq \beta, \\ 1 & \text{if } \alpha = \beta. \end{cases} \tag{12}$$

$\sigma_{\alpha\beta}$ is the cross-section [17, 18] of the (neutron producing) fusion reaction between $\alpha$ and $\beta$, and it enters as a function of the relative velocity $v_{\text{rel}}$ of the reactants. The statistical pre-factor containing the Kronecker delta evaluates to 1/2 for reactions between the same species (i.e. $\alpha$=$\beta$), and is necessary to avoid double-counting. Since this is a double integral over the velocity vectors of $\alpha$ and $\beta$, the integral is in principal six dimensional, which would be numerically too complex for a real-time calculation. Luckily,

there are several tricks to reduce the dimensionality. A rigorous derivation is given in [19], while we here just want to sketch the principle. First of all, the gyro-phase can be considered an ignorable coordinate of the distribution function, such that distribution functions are just given as 2D functions, e.g. of the speed $v$ and the pitch $\xi = v_\parallel/v$. The gyromotion is still important for calculating $v_{\mathrm{rel}}$, however, here only the relative gyrophase between $\alpha$ and $\beta$ is relevant. Therefore the integral can be reduced trivially to 5D. The distribution functions can be written as a series of Legendre polynomials $f_\alpha(v,\xi) = \sum_{l=0}^{\infty} f_{\alpha l}(v) P_l(\xi)$. Then the orthogonality of the Legendre polynomials $\int_{-1}^{1} P_n(\xi) P_m(\xi)\,\mathrm{d}\xi = \frac{2}{2n+1}\delta_{nm}$ can be exploited to reduce the dimensionality to 4D. As last step, one can use a fixed velocity grid for each species for the numerical implementation (with $N_{v\alpha}$ and $N_{v\beta}$ grid points, respectively). This allows to pre-compute one integration and hence reduce the dimensionality once more to the following triple sum:

$$r = \sum_{j=1}^{N_{v\alpha}} \sum_{j'=1}^{N_{v\beta}} \sum_{l=0}^{L} f_{\alpha l}(v_j) f_{\beta l}(v_{j'}) I_{jj'l} \tag{13}$$

with:

$$I_{jj'l} = c_j c_{j'} \frac{8\pi^2}{2l+1} v_j^2 v_{j'}^2 \sum_k P_l(\xi_k) c_k \sigma(u_{jj'k}) u_{jj'k} \tag{14}$$

$$u_{jj'k} = \sqrt{v_j^2 + v_{j'}^2 - 2 v_j v_{j'} \xi_k} \tag{15}$$

Here, $c_j$ are the coefficients of the numerical integration. This approach is also used in the TORIC-SSFPQL code package [20].

## 4 Implementation in RABBIT

### 4.1 Output of the distribution function

The above formulas suggest that we shall evaluate the NBI distribution function on a fixed velocity grid. This allows the slow computation of the coefficient matrix $I_{jj'l}$ to be carried out in advance, e.g. before the discharge and not in real-time, where computation time is not an issue. The fixed velocity grid is somewhat in contradiction to the numerical scheme of the time-dependence in RABBIT. As described above and in [14], here we follow a set of fast-ion pulses with a distinct $v_{\mathrm{start}}$ and $v_{\mathrm{final}}$ during each time-step, which are continuous and not given on a fixed grid. The distribution function $f$ for each pulse is given by the steady-state solution $f_{\mathrm{ss}}$ multiplied with a rectangular function $\mathrm{rect}(v) \equiv H(v - v_{\mathrm{final}}) \cdot H(v_{\mathrm{start}} - v)$, and the whole distribution function for a time-step is given as the sum of these Heaviside chunks.

Some care must be taken when mapping these Heaviside chunks onto the fixed velocity grid. The brute force approach of simply evaluating $\mathrm{rect}(v_j)$ at each velocity grid point can lead to large numerical errors when evaluating velocity integrals. This is illustrated

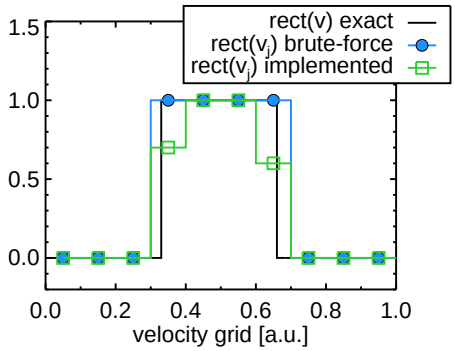


**Figure 2:** Illustration of the numerical scheme used for evaluating the rectangular functions on a fixed grid.

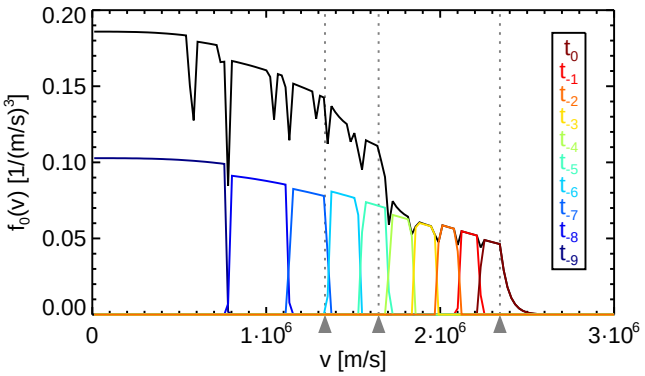


**Figure 3:** $l = 0$ component of the distribution function calculated by RABBIT (black line). With colors, the individual fast-ion pulses are shown for the highest energy component. The pulse with $t_0$ has been injected in the current time-step, $t_{-1}$ corresponds to ions injected in the previous time step and so forth. The beam in this example has three energy components (with a full, half and third fraction of the nominal injection energy of 60 keV - as it is usual for positive ion NBI). The three injection velocities are indicated with grey arrows and dashed lines. The black line corresponds to the full distribution function, i.e. including all three energy components.

by the blue curve in figure 2 for a mid-point rule integration in the case of the simple integral:

$$\int \mathrm{rect}(v)\mathrm{d}v = v_{\mathrm{start}} - v_{\mathrm{final}} \tag{16}$$

To eliminate this error, we multiply grid points which are only partially covered by the rectangular function with a corresponding proportional factor, such that the numerical result of $\int \mathrm{rect}(v)\mathrm{d}v$ (area under green curve) is equal to the exact result (area under black curve).

Figure 3 shows an example of a distribution function, for an ASDEX Upgrade case (#29783) with one active NBI source (Q3) at 60 keV injection energy in the plasma center. Plotted is the zero-th Legendre moment $f_0(v)$, which can be interpreted as the distribution function integrated over all pitches ($\int f \mathrm{d}\xi = 2f_0$). Due to the summation of the individual Heaviside chunks, the distribution function has some spikes. For the

highest injection velocity, the individual Heaviside chunks (i.e. fast ion pulses) are plotted with colors corresponding to their "age": $t_0$ in the legend corresponds to a fast-ion pulse which has been injected in the current time-step, $t_{-1}$ corresponds to ions which have been injected in the previous time step and so forth. The older such a pulse is, the further it has already slowed down. The time-step in this example is 5 ms and there are 10 fast-ion pulses to be seen, corresponding to a slowing down time of approximately 50 ms.

For each energy component of the beam, the fast-ion pulse with the highest velocity is corrected for the effect of speed diffusion. The latter is a diffusive process with respect to the speed $v$. It is weak where $f_0(v)$ has low gradients (i.e. below the injection energy). Therefore, it is neglected in RABBIT below the injection energy (see $f_-$, eq. 7). Above the injection energy, however, a strong gradient (the last step of the Heaviside function) results in a strong diffusion towards velocities above the injection energy. This is modeled by smoothly appending an appropriate exponential decay $f_+$ (8) for energies above the injection energy. This small correction is considered to be instantaneously in steady-state, i.e. a time-dependent build-up of this tail is currently neglected. Comparisons with NUBEAM show that indeed this build-up is much faster than the slowing-down time, such that this seems to be an acceptable approximation [14].

Due to the time-dependence scheme, which involves a summation over individual Heaviside chunks, the distribution function is not necessarily smooth and gradients are not well defined everywhere. This may happen due to the following reasons: 1) The source rate may vary between two following fast-ion pulses. Note that even if the injected NBI power remains constant, the deposition into a given radial bin may change due to local changes of the birth profile. 2) The parameters in the Fokker-Planck (FP) equation $\tau_s(v,t)$, $v_c(v,t)$ and $\beta(v,t)$ are a function of plasma parameters (hence a function of $t$). In addition, we take into account Coulomb-logarithms that depend on the fast-ion velocity $v$ [14], such that $\tau_s$, $v_c$ and $\beta$ are also a weak function of $v$. It should be noted that the analytic solutions $f_+$ and $f_-$ are derived neglecting this $v$-dependence. Since we evaluate these solutions only in small Heaviside-chunks, we can evaluate $\tau_s$, $v_c$ and $\beta$ individually for each chunk, which leads to a more accurate result (of e.g. the moments) but also to a less smooth output of the distribution function.

In the given example (fig. 3) the changing FP parameters are the dominant mechanism for creating the gaps: The output has been created shortly after the NBI onset, where the fast-ion density is not yet in steady state. Increasing fast-ion density leads to increasing dilution of the plasma and hence to changes in $\tau_s$, $v_c$ and $\beta$ that lead to increasingly weaker slowing down. This is why 'gaps' open up between consecutive Heaviside chunks in this example. Figure 4a shows an example where we ensured, that all inputs (such as equilibrium and plasma parameters) are constant. The remaining non-smoothness is due to the $v$-dependence of the FP parameters ($\tau_s$, $v_c$ and $\beta$).

To conclude, providing realistic time-dependent gradients of the distribution function is currently out of the scope of RABBIT. Instead, the numerical scheme is optimized for calculating integrals of the distribution function (such as the neutron rate). A different numeric scheme might cure non-smoothness coming from reason 2), but varying source rates (reason 1) would still lead to non-physical gradients. This is due to the neglection of speed-diffusion, which would smooth out the edges of the Heaviside chunks. Hence,

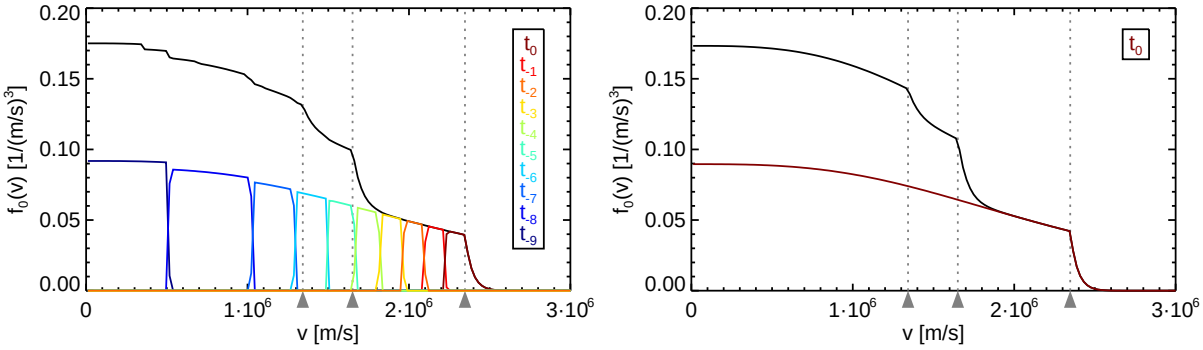


**Figure 4:** Smoother distribution functions are obtained under steady-state conditions. Left: Case with time-constant inputs (but $v$-dependent FP parameters). Right: Solution in the limit of infinite time-step $\Delta t \to \infty$.

RABBIT is anyway missing the physics to provide realistic time-dependent gradients of $f$.

One could obtain smooth distribution functions and hence realistic gradients by enforcing steady-state conditions $\frac{\partial f}{\partial t} = 0$. Technically, this can be done easily by letting the time-step $\Delta t \to \infty$. The resulting distribution is shown in fig. 4b. In addition to omitting the time-dependence, it also does no longer contain the $v$-dependence of $\tau_s$, $v_c$ and $\beta$. In turn, this 'steady-state' operation mode would allow to calculate gradients, which might be relevant e.g. for MHD stability calculations.

## 4.2 Number of Legendre components

As next question, we consider how many Legendre components (i.e. $l$-terms) are necessary in the triple sum (13). The present RABBIT version implements only $l = 0, 1$ (i.e. $L = 1$), because those are sufficient for calculating moments of e.g. density, heating, scalar pressure (all $l = 0$) and current-drive ($l = 1$). While it is, in principle, straight forward to implement higher $l$s aswell, it is of particular interest if $L = 1$ is already sufficient. We consider the most common case in present day devices, which is injection of deuterium beams into a deuterium plasma. It is illustrative to consider separate species for thermal deuterium and fast (or beam) deuterium, as shown in table 1. The thermal

| Species $\alpha$ | Species $\beta$ | Name | remark on $f$ | exact result for: |
|---|---|---|---|---|
| thermal | thermal | thermo-nuclear | $f_{\alpha l} = 0 = f_{\beta l}$ for $l > 0$ | $L = 0$ |
| thermal | beam | beam-target | $f_{\alpha l} = 0$ for $l > 0$ | $L = 0$ |
| beam | beam | beam-beam | only here we need $l > 0$ | $L = \infty$ |

**Table 1:** Overview and nomenclature of neutron production channels between a thermal and a fast (beam) species.

species (or the thermal part of the distribution function) is isotropic. This is true also in the case of finite toroidal rotation, because RABBIT considers the frame of reference rotating with the plasma. It means that $f_\alpha$ is not a function of $\xi$. Since we write $f_\alpha$ as series

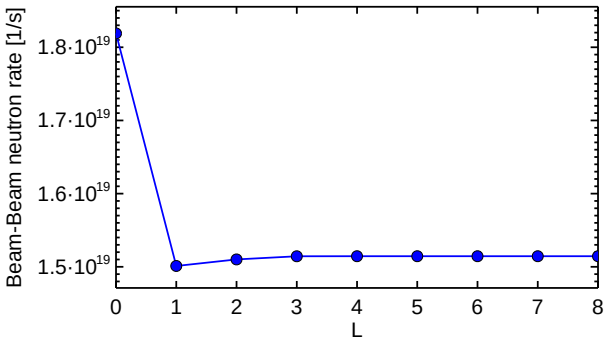


**Figure 5:** Beam-beam neutron rate as function of $L$ ($l = 0, \ldots, L$.)

of Legendre polynomials ($f_\alpha(v,\xi) = \sum_{l=0}^{\infty} f_{\alpha l}(v) P_l(\xi)$) and since $P_l(\xi)$ is a polynomial of order $l$, any isotropic distribution must have $f_{\alpha l}(v) = 0$ for $l > 0$. In the neutron rate triple sum (eq. 13), the product $f_{\alpha l}(v) \cdot f_{\beta l}(v)$ enters, where only the $f_{\alpha 0}(v) \cdot f_{\beta 0}(v)$ term survives if one of the two distribution functions is isotropic. This means that for the thermo-nuclear and beam-target contribution we get exact neutron rates already with $L = 0$. This is encouraging, because in typical present-day plasmas, beam-target is the dominant neutron production mechanism, while beam-beam neutrons are usually in the order of or below 10%. We further investigate this with an ASDEX Upgrade test case with one NBI (Q3) at 60 keV.

Fig. 5 shows the volume integrated beam-beam neutron emission calculated as function of $L$. There is a relatively strong change going from $L = 0$ to $L = 1$, but afterwards, almost no change is observable towards higher $L$. To understand this, one needs to remember that $P_l(\xi)$ is a polynomial of $\xi$ to the power $l$. $L = 0$ corresponds to a isotropic distribution. The first moment ($P_1(\xi) = \xi$) contains information about the average pitch:

$$\langle \xi \rangle (v) = \frac{\int f \xi \mathrm{d}\xi}{\int f \mathrm{d}\xi} = \frac{f_1}{3 f_0} \tag{17}$$

At first sight, it may seem counter-intuitive, that the average pitch has an effect on the neutron rates at all: Since the fusion reactivity depends on the relative velocity $v_{\mathrm{rel}}$ of the reactants, one expects large neutron yield if the velocity vectors are different to each other, independent of the average direction. Considering particles with same speed, one might think that the variance of the pitch distribution is more important than its mean value. However, one must not forget about the gyro-motion. Particles with $\xi = v_\parallel / v = 1$ do not gyrate at all ($v_\perp = 0$), have all the same velocity vector (at same speed) and hence a lowered fusion probability. Particles with $\xi = 0$, on the other side, are purely gyrating, which bears the possibility of large variations in the velocity vector (at same speed), up to opposing velocity vectors. This is the main reason why the average pitch of the distribution function adds a quite large correction with respect to the $L = 0$ term.

In this example for realistic ASDEX Upgrade conditions (based on discharge #29783), the error of the beam-beam neutron rate, taking only $L = 1$, is below 1%. In addition, the beam-beam neutrons contribute only 15 % locally in the core (see fig. 6), or 10% volume-integrated to the total neutron rate, such that the error in the latter is further reduced to 0.1% and hence insignificant. We conclude that $L = 1$ is sufficient, which

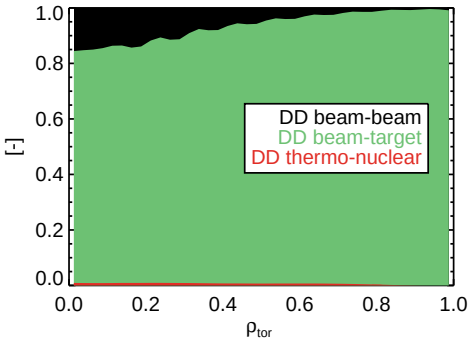


**Figure 6:** Composition of the neutron emission profile for AUG #29783 3.44 s (according to NUBEAM).

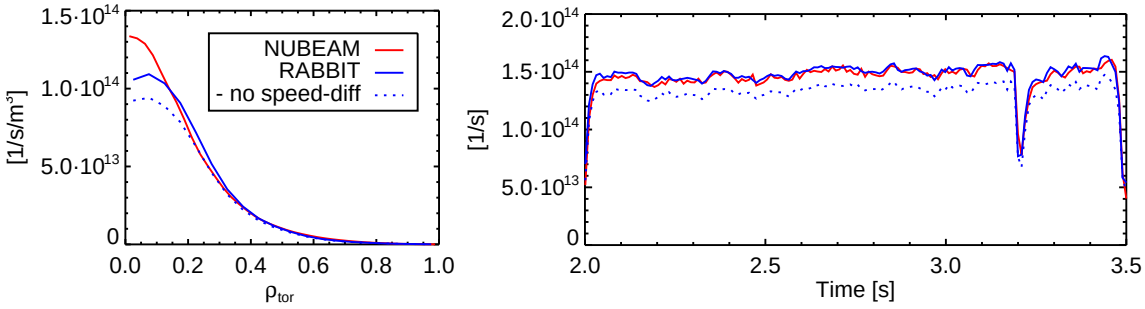


**Figure 7:** ASDEX Upgrade benchmark case. Left: Neutron emission profile at 3.11 s, right: Volume-integrated time trace. The dashed line corresponds to a RABBIT run with deactivated effect of speed-diffusion.

effectively reduces the triple sum (13) to two double sums. This is fast enough for real time applications, even with a relatively fine velocity mesh, e.g. $N_{v\alpha} = N_{v\beta} = 150$.

## 5 Benchmark cases

### 5.1 ASDEX Upgrade

Fig. 7 shows a benchmark between NUBEAM and RABBIT for the neutron emission profile for the above case. The agreement in the profile shapes is good and the volume integrated neutron rate matches very well. For comparison, the dashed curve corresponds to a RABBIT-run where the speed-diffusion correction was deactivated. Despite moderate bulk temperatures ($T_\mathrm{e} \approx 2.9\,\mathrm{keV}$, $T_\mathrm{i} \approx 1.6\,\mathrm{keV}$ in the core) the speed-diffusion has a 10% effect on the neutron rates, and the agreement is much better when including this effect. The number of particles in this high energy tail may be small, but they have high energies, and thus are over-proportionally relevant for the neutron production.

### 5.2 JET

For the JET tokamak we have analyzed discharge #92436, which is a high-performance pure deuterium discharge. 15 out of 16 NBI sources were used (28 MW), and an additional amount of 5 MW ion cyclotron resonance heating (ICRH) was applied. ICRH is mainly

absorbed by a hydrogen minority at the first harmonic frequency, but there is also a finite amount absorbed by the beam ions at the second harmonic. This leads to a further acceleration of the beam ions and hence has an effect on the neutron rate. For a fair comparison with RABBIT, we first compare it with a TRANSP run where this NBI-RF synergy is switched off. The resulting neutron timetraces are shown with solid lines in fig. 8. It can be seen that the agreement between RABBIT and TRANSP is excellent, and the two lines are almost indistinguishable. Also the profile of neutron emission (fig. 9) agrees very well.

There are several reasons why the agreement is so good in this case: Firstly, up to 50% of the neutrons are caused by thermo-nuclear fusion in this case, for which RABBIT and TRANSP use exactly the same formulas and cross-sections [17, 18]. Secondly, the approximations in RABBIT (e.g. the ad-hoc treatment of finite orbit widths and the neglection of collisional transport) are likely better fulfilled on larger devices than on smaller ones. In addition, the excellent agreement here is a bit by chance, due to two differences between the RABBIT and NUBEAM runs, which tend to cancel out each other here: RABBIT can currently only treat one main ion species (D in this case) and one impurity species (nickel in this case), while NUBEAM takes in addition the hydrogen minority ($n_\mathrm{H}/n_\mathrm{e}$=1.7%) into account. This leads to a weak dilution (lower Deuterium density) and hence a reduced neutron rate in TRANSP. For the thermo-nuclear part, the dilution leads to a quadratic reduction of the neutron rates, whereas for beam-target it enters linearly. In total, it results in approximatively a 2-3% reduction of neutron rates in the TRANSP result. In addition, NUBEAM tracks the tritium which is born from DD reactions. It can consequently do DT fusion and emit additional neutrons, which contribute 2% in the TRANSP calculation. They therefore replace the "missing" neutrons due to hydrogen dilution (compare fig. 8). In any case, both effects are small such that even if they would not cancel each other, the agreement between RABBIT and TRANSP still would be good.

The NBI-ICRH synergy has a clearer effect on the neutron rates in this case. In NUBEAM, this is calculated with an RF kick operator [21, 22] based on the wave fields from TORIC [23]. The kick operator is still under development [24], first comparisons with experiments indicate however already a reasonable agreement [25, 26]. In the future, it might be interesting to couple RABBIT with a to be developed real-time capable ICRH code. Then, the high-energy tail in the beam ion distribution resulting from this synergy might be added in the RABBIT distribution function, such that this synergy could be taken into account.

## 6 Application on DIII-D

For a first test and application of the RABBIT code at DIII-D, we have written an automatic script, which takes the shot-number as only input. The script reads then the equilibrium reconstruction from the EFIT code [27], the plasma profiles from automatic fits done with ZipFit [28] and the NBI parameters for the given shot on a timebase with 20 ms resolution. It writes the inputs into ASCII files, starts the RABBIT calculation and reads the outputs. The total calculation takes around one minute, whereby at least half of the time is spent on preparing the input files. Hence, this tool allows for fast intershot

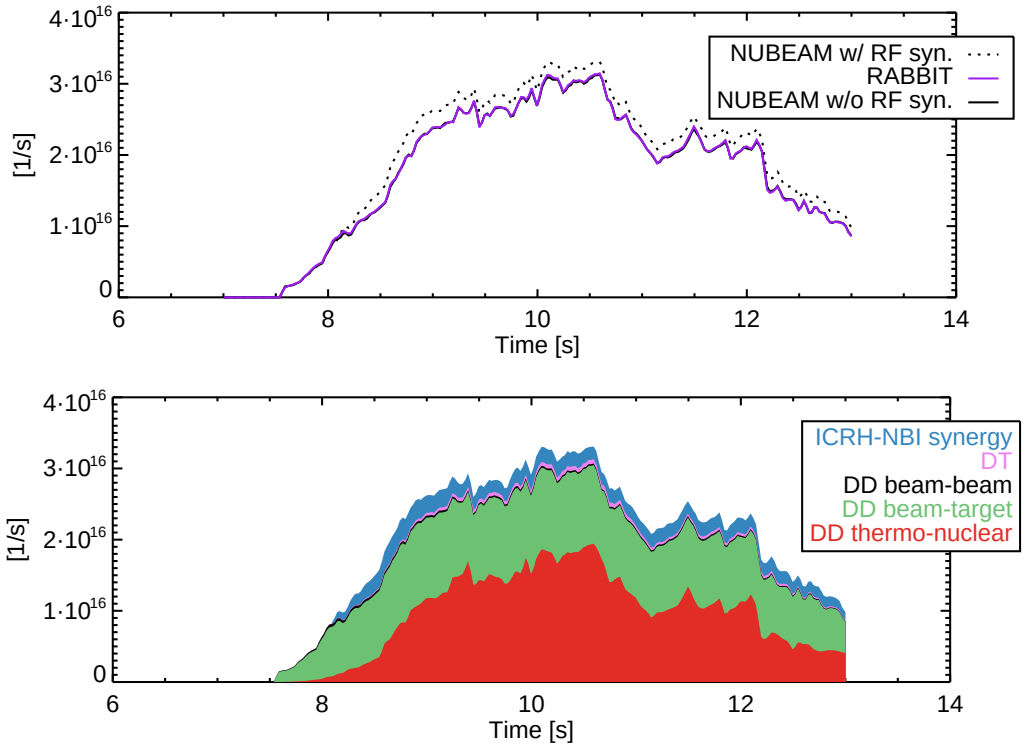


**Figure 8:** JET benchmark case. Top: Volume-integrated neutrons. The NUBEAM NBI-only result (i.e. without ICRF-NBI synergetic effects) agrees almost perfectly with RABBIT. Bottom: Composition of the neutron rates according to NUBEAM.

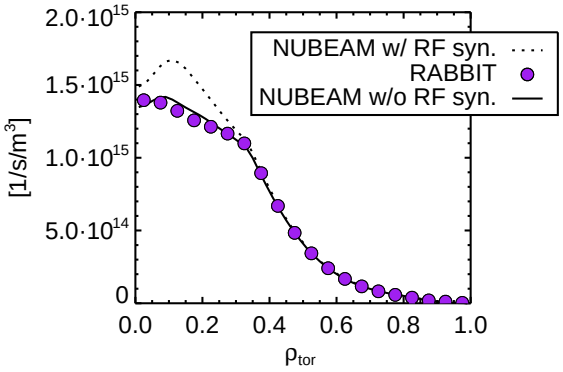


**Figure 9:** Neutron emission profiles at 9.52 s. The agreement between RABBIT and NUBEAM (NBI-only) is excellent.

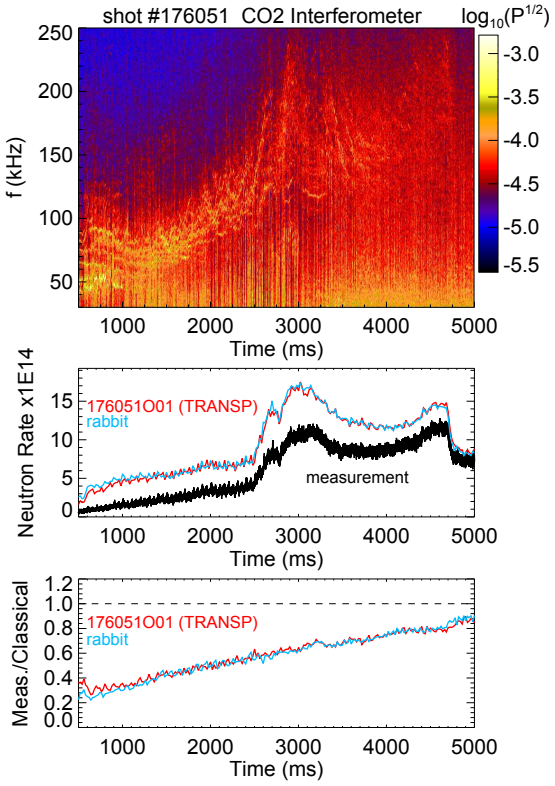


**Figure 10:** Top: Spectrogram of a CO2 Interferometer. Middle: Measured neutron rates in comparison to neo-classical prediction from RABBIT and TRANSP. Bottom: Ratio between measured neutron rate and neo-classical predictions. The strong mismatch between both can be explained by the strong Alfvén eigenmode activity in this discharge (as seen in the top plot).

analysis, and the information can be already incorporated for the decision-making of the next discharge.

A similar workflow was recently established for TRANSP - the BEAST operation mode (between and amongst shots TRANSP) [29]. Here, temporal and spatial resolution and in particular the number of Monte Carlo markers in NUBEAM are lowered to achieve a lower computation time. The spatial (20 grid points) and temporal (20 ms) resolution is equal to the RABBIT parameters, but the calculation time is still much larger. According to [29], one second of tokamak time requires 0.3 hours of computation time. A typical DIII-D discharge with 5 s hence still needs 1.5 hours, which is much longer than the typical time between two consecutive discharges. Analysis results can hence not be used for the next discharge, but only some discharges later-on. The inputs for these BEAST-TRANSP runs are essentially the same as for RABBIT, which allows for a verification of the RABBIT runs.

Both approaches have been applied during experiments for the development of high-performance steady-state advanced scenarios at DIII-D [30]. These scenarios feature a reversed shear in the core, with a minimum of the safety factor $q_{\min} > 2$ leading to the presence of Alfvén eigenmodes (AE) which can degrade the plasma performance strongly [31]. Figure 10 shows experimental data from one of the shots. The first plot shows

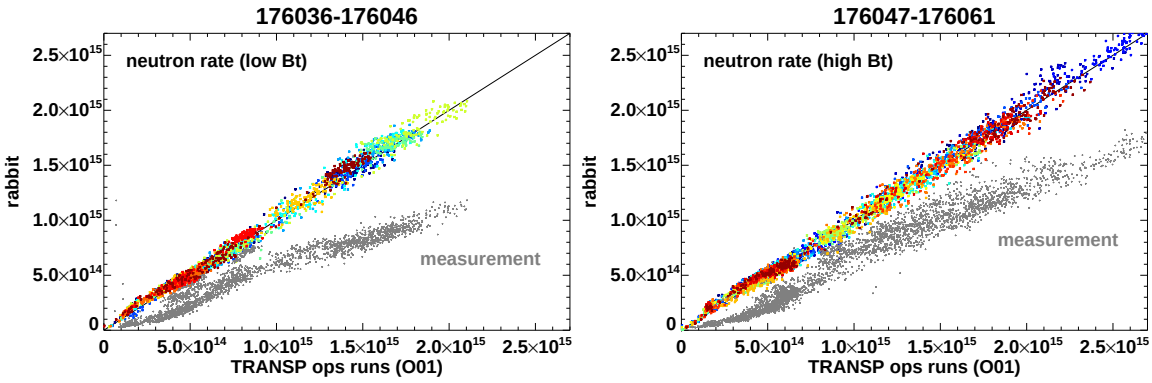


**Figure 11:** Database comparison between RABBIT and BEAST-TRANSP runs for a steady-state experimental session on DIII-D. The agreement between both codes is good, both for low-$B_t$ (1.75 T, left) and high-$B_t$ (2.0 T, right) cases. Data points within the same discharge are plotted with same color. The measurements fall short, because there was significant AE activity in almost all shots and timepoints.

a spectrogram of an interferometer, and strong AE activity is clearly observed. In the second plot a comparison between measured and neo-classically predicted neutron rates is shown. The measured neutron rates fall short significantly. This becomes even more clear in the third plot, where the ratio between measurement and neo-classical prediction is shown. This neutron rate short-fall can be used to quantify the fast-ion confinement degradation due to the AEs. The neutron rate predictions with RABBIT and TRANSP agree very well, such that with RABBIT the same information is available much faster (within few minutes) after the discharge.

Since both the RABBIT and BEAST codes were run automated during the whole experimental session, we could compile a larger database as shown in fig. 11. The data points align nicely along the diagonal, such that the RABBIT and TRANSP results are in good agreement.

## 7 Summary and outlook

In this paper, we describe the calculation of neutron emission in the RABBIT code. It is defined as a six dimensional integral over the two velocity spaces of the colliding species. The usage of a fixed velocity grid allows a reduction to a triple sum and hence an efficient and real-time capable evaluation.

As spin-off of this approach, RABBIT has now a module to output the distribution function directly. This might be of interest for direct comparison with fast-ion diagnostics, such as the FIDA diagnostic. It might also be of interest for measuring main-ion properties (temperature, rotation, density) from the $D_\alpha$ spectrum [32–34], which requires a subtraction or fitting of the FIDA component of the spectrum. The main limitation at this stage is that RABBIT currently calculates only the flux-surface averaged distribution function $\langle f \rangle$, whereas for a diagnostic application, one would typically need localized estimates in the $(R, z)$ plane. A sensitivity study could clarify, if $\langle f \rangle$ is already good enough for certain applications. An $(R, z)$-resolved distribution function could be

obtained from changing the mapping during the orbit-average: Instead of mapping onto a radial grid, one could map into a 2D ($R$, $z$)-matrix.

In addition, the distribution function could be of interest for MHD stability analysis. Here, typically the gradients of $f$ are relevant. We have shown that RABBIT could provide well-defined gradients for steady-state solutions.

We have tested the neutron calculations on several benchmark cases on ASDEX Upgrade, JET and DIII-D and found good agreement. At DIII-D, the neo-classical neutron prediction from RABBIT was already used for a fast intershot analysis of fast-ion transport due to Alfvén eigenmodes (AE). A decline of fast-ion confinement and hence discharge performance can be detected by a short-fall of the measured neutron rate with respect to the prediction. This has been used during an experimental session for the development of advanced steady-state scenarios with reversed shear. These scenarios are prone to strong AE activity, and the goal is to limit the detrimental effect of the AEs and to optimize the discharge performance. With RABBIT, this information is available within minutes after the discharge such that better decisions can be made for the following discharge. A later carried out comparison with TRANSP runs for the whole experimental session revealed a good agreement.

In order to make these new modeling capabilities available for a large userbase, it is ongoing work to include RABBIT into integrated modeling frameworks such as OMFIT [35] and IMAS [36]. The fast-ion profiles from RABBIT are already used within the IDE code [37] for improved equilibrium reconstructions [38]. In addition, RABBIT is coupled to the transport codes ASTRA [39, 40] and RAPTOR [41, 42], which will allow applications e.g. for discharge planning [43], reactor concept studies and in real time [41, 44].

It has recently been outlined in [45] that the neutron predictions from RABBIT could be used in real-time for AE control experiments. Since DIII-D has a real-time capable neutron diagnostic, one could estimate the loss of confinement and discharge performance (compared to the neo-classical prediction) during the discharge. In conjunction with direct AE detection with ECE diagnostics, when detrimental conditions are observed, countermeasures to stabilize the AEs could be activated during the discharge. The demonstration of such control techniques might be of great importance for future fusion reactors, where strong AE activity is expected.

## Acknowledgments

We acknowledge F. Felici, R. Fischer and B. Geiger for encouraging the development of RABBIT. We greatly thank R. Dux and A. Lebschy for providing the NBI attenuation calculation from the BESFM code [46], which was the starting point for the development of RABBIT. We thank M. Fitzgerald, H.-T. Kim and D. King who have prepared the TRANSP runs for the JET benchmark case. The DIII-D BEAST-TRANSP runs were performed using the OMFIT integrated modeling framework [35].

This work has been carried out within the framework of the EUROfusion Consortium and has received funding from the Euratom research and training programme 2014-2018 under grant agreement No 633053. The views and opinions expressed herein do not necessarily reflect those of the European Commission.

This material is based upon work supported in part by the U.S. Department of Energy, Oce of Science, Oce of Fusion Energy Sciences, using the DIII-D National Fusion Facility,

a DOE Oce of Science user facility, under Awards DE-FC02-04ER54698, SC-G903402, DE-AC02-09CH11466, DE-AC05-00OR22725. DIII-D data shown in this paper can be obtained in digital format by following the links at https://fusion.gat.com/global/D3D_DMP.

## References

[1] W. Heidbrink and G. Sadler. The behaviour of fast ions in tokamak experiments. *Nuclear Fusion*, 34(4):535, 1994.

[2] B. Geiger. *Fast-ion transport studies using FIDA spectroscopy at the ASDEX Upgrade tokamak*. Phd thesis, LMU München, 2013. also IPP report 10/46.

[3] M. Weiland, B. Geiger, A. S. Jacobsen, M. Reich, M. Salewski, T. Odstrčil, and the ASDEX Upgrade Team. Enhancement of the FIDA diagnostic at ASDEX Upgrade for velocity space tomography. *Plasma Physics and Controlled Fusion*, 58(2):025012, 2016.

[4] M. Weiland, R. Bilato, B. Geiger, P. Schneider, G. Tardini, M. Garcia-Muñoz, F. Ryter, M. Salewski, H. Zohm, et al. Phase-space resolved measurement of 2nd harmonic ion cyclotron heating using FIDA tomography at the ASDEX Upgrade tokamak. *Nuclear Fusion*, 57(11):116058, 2017.

[5] R. J. Goldston, D. McCune, H. Towner, S. Davis, R. Hawryluk, and G. Schmidt. New techniques for calculating heat and particle source rates due to neutral beam injection in axisymmetric tokamaks. *Journal of computational physics*, 43(1):61–78, 1981.

[6] A. Pankin, D. McCune, R. Andre, G. Bateman, and A. Kritz. The tokamak Monte Carlo fast ion module NUBEAM in the National Transport Code Collaboration library. *Computer Physics Communications*, 159(3):157 – 184, 2004.

[7] F. Poli, J. Sachdev, J. Breslau, M. Gorelenkova, and X. Yuan. TRANSP. [Computer Software] `https://dx.doi.org/10.11578/dc.20180627.4`, jun 2018.

[8] H. Duong, W. Heidbrink, E. Strait, T. Petrie, R. Lee, R. Moyer, and J. Watkins. Loss of energetic beam ions during TAE instabilities. *Nuclear Fusion*, 33(5):749, 1993.

[9] M. Garcia-Munoz, I. Classen, B. Geiger, W. Heidbrink, M. V. Zeeland, S. Äkäslompolo, R. Bilato, V. Bobkov, M. Brambilla, G. Conway, S. da Graça, V. Igochine, P. Lauber, N. Luhmann, M. Maraschek, F. Meo, H. Park, M. Schneller, G. Tardini, and the ASDEX Upgrade Team. Fast-ion transport induced by Alfvén eigenmodes in the ASDEX Upgrade tokamak. *Nuclear Fusion*, 51(10):103013, 2011.

[10] M. A. Van Zeeland, W. W. Heidbrink, R. K. Fisher, M. García Muñoz, G. J. Kramer, D. C. Pace, R. B. White, S. Aekaeslompolo, M. E. Austin, J. E. Boom, I. G. J. Classen, S. da Graça, B. Geiger, M. Gorelenkova, N. N. Gorelenkov, A. W. Hyatt, N. Luhmann, M. Maraschek, G. R. McKee, R. A. Moyer, C. M. Muscatello,

R. Nazikian, H. Park, S. Sharapov, W. Suttrop, G. Tardini, B. J. Tobias, and Y. B. Zhu. Measurements and modeling of Alfvén eigenmode induced fast ion transport and loss in DIII-D and ASDEX Upgrade. *Physics of Plasmas*, 18(5):056114, 2011.

[11] C. Collins, W. Heidbrink, M. Podestà, R. White, G. Kramer, D. Pace, C. Petty, L. Stagner, M. V. Zeeland, Y. Zhu, and T. D.-D. Team. Phase-space dependent critical gradient behavior of fast-ion transport due to Alfvén eigenmodes. *Nuclear Fusion*, 57(8):086005, 2017.

[12] M. Ishikawa, M. Takechi, K. Shinohara, Y. Kusama, C. Cheng, G. Matsunaga, Y. Todo, N. Gorelenkov, G. Kramer, R. Nazikian, A. Fukuyama, V. Krasilnikov, Y. Kashuck, T. Nishitani, A. Morioka, M. Sasao, M. Isobe, and the JT-60 team. Energetic ion transport by abrupt large-amplitude event induced by negative-ion-based neutral beam injection in the JT-60U. *Nuclear Fusion*, 45(12):1474, 2005.

[13] M. Cecconello, O. M. Jones, W. U. Boeglin, R. V. Perez, D. S. Darrow, et al. Energetic ion behaviour in MAST. 57:014006, 2015.

[14] M. Weiland, R. Bilato, R. Dux, B. Geiger, A. Lebschy, F. Felici, R. Fischer, D. Rittich, M. van Zeeland, the ASDEX Upgrade Team, and the Eurofusion MST1 Team. RABBIT: Real-time simulation of the NBI fast-ion distribution. *Nuclear Fusion*, 58(8):082032, 2018.

[15] J. G. Cordey and W. G. F. Core. Energetic particle distribution in a toroidal plasma with neutral injection heating. *Physics of Fluids*, 17(8), 1974.

[16] J. D. Gaffey. Energetic ion distribution resulting from neutral beam injection in tokamaks. *Journal of Plasma Physics*, 16(2):149–169, 1976.

[17] H.-S. Bosch and G. Hale. Improved formulas for fusion cross-sections and thermal reactivities. *Nuclear Fusion*, 32(4):611, 1992.

[18] H.-S. Bosch and G. Hale. Improved formulas for fusion cross-sections and thermal reactivities. *Nuclear Fusion*, 33(12):1919, 1993.

[19] J. Cordey, K. Marx, M. McCoy, A. Mirin, and M. Rensink. A new expansion method for computing $\sigma v$ for reactant distribution functions. *Journal of Computational Physics*, 28(1):115 – 121, 1978.

[20] R. Bilato, M. Brambilla, O. Maj, L. Horton, C. Maggi, and J. Stober. Simulations of combined neutral beam injection and ion cyclotron heating with the TORIC-SSFPQL package. *Nuclear Fusion*, 51(10):103034, 2011.

[21] J.-M. Kwon, C. Chang, S.-H. Ku, D. McCune, and C. Phillips. Development of XGC-RF for Global Guiding-Center Particle Simulation of minority ICRH heated Plasmas in a General Tokmak Geometry. *Bulletin of the American Physical Society, 48th meeting of the Division of Plasma Physics, Philadelphia (PA)*, 2006.

[22] J.-M. Kwon, D. McCune, and C. Chang. Enhancement of NUBEAM for the simulation of fast ion and RF-wave interaction based on the quasi-linear theory. *Bulletin of the American Physical Society, 49th meeting of the Division of Plasma Physics, Orlando (FL)*, 2007.

[23] M. Brambilla. Numerical simulation of ion cyclotron waves in tokamak plasmas. *Plasma Physics and Controlled Fusion*, 41(1):1–34, jan 1999.

[24] N. Bertelli, E. Valeo, D. Green, M. Gorelenkova, C. Phillips, M. Podestà, J. Lee, J. Wright, and E. Jaeger. Full-wave simulations of ICRF heating regimes in toroidal plasma with non-Maxwellian distribution functions. *Nuclear Fusion*, 57(5):056035, apr 2017.

[25] M. Weiland, R. Bilato, B. Geiger, P. Schneider, G. Tardini, M. Garcia-Muñoz, F. Ryter, M. Salewski, H. Zohm, and and. Phase-space resolved measurement of 2nd harmonic ion cyclotron heating using FIDA tomography at the ASDEX Upgrade tokamak. *Nuclear Fusion*, 57(11):116058, aug 2017.

[26] G. Tardini, R. Bilato, R. Fischer, and M. W. and. Detection of neutral beam deuterons acceleration by 2nd harmonic radio frequency heating in ASDEX Upgrade via neutron spectrometry. *Nuclear Fusion*, 59(4):046002, jan 2019.

[27] L. Lao, H. S. John, R. Stambaugh, A. Kellman, and W. Pfeiffer. Reconstruction of current profile parameters and plasma shapes in tokamaks. *Nuclear Fusion*, 25(11):1611, 1985.

[28] Q. Peng, R. J. Groebner, L. L. Lao, J. Schachter, D. P. Schissel, and M. R. Wade. Status of the Linux PC cluster for between-pulse data analyses at DIII-D. *Fusion Engineering and Design*, 60, 06 2002.

[29] B. A. Grierson, X. Yuan, M. Gorelenkova, S. Kaye, N. C. Logan, O. Meneghini, S. R. Haskey, J. Buchanan, M. Fitzgerald, S. P. Smith, L. Cui, R. V. Budny, and F. M. Poli. Orchestrating TRANSP Simulations for Interpretative and Predictive Tokamak Modeling with OMFIT. *Fusion Science and Technology*, 74(1-2):101–115, 2018.

[30] C.S. Collins et. al. *APS Conference*, 2018.

[31] W. W. Heidbrink, J. R. Ferron, C. T. Holcomb, M. A. Van Zeeland, X. Chen, C. S. Collins, A. Garofalo, X. Gong, B. A. Grierson, M. Podestà, L. Stagner, and Y. Zhu. Confinement degradation by Alfven-eigenmode induced fast-ion transport in steady-state scenario discharges. 56:095030, 2014.

[32] B. A. Grierson, K. H. Burrell, C. Chrystal, R. J. Groebner, D. H. Kaplan, W. W. Heidbrink, J. M. Muñoz Burgos, N. A. Pablant, W. M. Solomon, and M. A. Van Zeeland. Active spectroscopic measurements of the bulk deuterium properties in the DIII-D tokamak (invited). *Review of Scientific Instruments*, 83(10):10D529, 2012.

[33] B. A. Grierson, K. H. Burrell, C. Chrystal, R. J. Groebner, S. R. Haskey, and D. H. Kaplan. High resolution main-ion charge exchange spectroscopy in the DIII-D H-mode pedestal. *Review of Scientific Instruments*, 87(11):11E545, 2016.

[34] S. R. Haskey, B. A. Grierson, K. H. Burrell, C. Chrystal, R. J. Groebner, D. H. Kaplan, N. A. Pablant, and L. Stagner. Measurement of deuterium density profiles in the H-mode steep gradient region using charge exchange recombination spectroscopy on DIII-D. *Review of Scientific Instruments*, 87(11):11E553, 2016.

[35] O. Meneghini, S. Smith, L. Lao, O. Izacard, Q. Ren, J. Park, J. Candy, Z. Wang, C. Luna, V. Izzo, B. Grierson, P. Snyder, C. Holland, J. Penna, G. Lu, P. Raum, A. McCubbin, D. Orlov, E. Belli, N. Ferraro, R. Prater, T. Osborne, A. Turnbull, and G. Staebler. Integrated modeling applications for tokamak experiments with OMFIT. *Nuclear Fusion*, 55(8):083008, 2015.

[36] F. Imbeaux, S. Pinches, J. Lister, Y. Buravand, T. Casper, B. Duval, B. Guillerminet, M. Hosokawa, W. Houlberg, P. Huynh, S. Kim, G. Manduchi, M. Owsiak, B. Palak, M. Plociennik, G. Rouault, O. Sauter, and P. Strand. Design and first applications of the ITER integrated modelling & analysis suite. *Nuclear Fusion*, 55(12):123006, oct 2015.

[37] R. Fischer, A. Bock, M. Dunne, J. C. Fuchs, L. Giannone, K. Lackner, P. J. McCarthy, E. Poli, R. Preuss, M. Rampp, M. Schubert, J. Stober, W. Suttrop, G. Tardini, M. Weiland, and A. U. Team. Coupling of the Flux Diffusion Equation with the Equilibrium Reconstruction at ASDEX Upgrade. *Fusion Science and Technology*, 69(2):526–536, 2016.

[38] R. Fischer, A. Bock, A. Burckhart, O. Ford, L. Giannone, V. Igochine, M. Weiland, and M. W. and. Sawtooth induced q-profile evolution at ASDEX Upgrade. *Nuclear Fusion*, 59(5):056010, mar 2019.

[39] G. V. Pereverzev and P. Yushmanov. ASTRA. Automated System for TRansport Analysis in a tokamak. 2002.

[40] E. Fable, C. Angioni, F. J. Casson, D. Told, A. A. Ivanov, F. Jenko, R. M. McDermott, S. Y. Medvedev, G. V. Pereverzev, F. Ryter, W. Treutterer, and E. V. and. Novel free-boundary equilibrium and transport solver with theory-based models and its validation against ASDEX Upgrade current ramp scenarios. *Plasma Physics and Controlled Fusion*, 55(12):124028, nov 2013.

[41] F. Felici, O. Sauter, S. Coda, B. Duval, T. Goodman, J. Moret, J. Paley, T. Team, et al. Real-time physics-model-based simulation of the current density profile in tokamak plasmas. *Nuclear Fusion*, 51(8):083052, 2011.

[42] F. Felici and O. Sauter. Non-linear model-based optimization of actuator trajectories for tokamak plasma profile control. *Plasma Physics and Controlled Fusion*, 54(2):025002, 2012.

[43] W. Treutterer, E. Fable, A. Gräter, F. Janky, O. Kudlacek, I. G. Ortiz, T. Maceina, G. Raupp, B. Sieglin, and T. Zehetbauer. Concepts of the new ASDEX Upgrade flight simulator. *Fusion Engineering and Design*, 2019.

[44] B. Sieglin, W. Treutterer, and L. Giannone. DCS satellite: Enhanced plant system integration on ASDEX Upgrade. *Fusion Engineering and Design*, 2019.

[45] W. Hu, K. Olofsson, A. Welander, W. Heidbrink, M. V. Zeeland, M. Austin, C. Collins, D. Humphreys, E. Kolemen, J. Li, B. Xiao, and D.-D. Team. Active real-time control of Alfvén eigenmodes by neutral beam and electron cyclotron heating in the DIII-D tokamak. *Nuclear Fusion*, 58(12):124001, 2018.

[46] A. Lebschy. *Electron density reconstruction using beam emission spectroscopy on a heating beam.* Master thesis, LMU München, 2014.